Research Article | Vol. 30, No. 10 / 9 May 2022 / Optics Express 16020
Optics EXPRESS

Ultra-narrow-band circular dichroism by surface lattice resonances in an asymmetric dimer-on-mirror metasurface

JIGANG HU,[1] YUXI XIAO,[1] LEI-MING ZHOU,[1,*] XIAOYUN JIANG,[1] WEI QIU,[1] WU FEI,[1] YANG CHEN,[2] AND QIWEN ZHAN[3,4]

[1]Department of Optical Science and Engineering, Hefei University of Technology, Hefei, Anhui 230009, China
[2]CAS Key Laboratory of Mechanical Behavior and Design of Materials, Department of Precision Machinery and Precision Instrumentation, University of Science and Technology of China, Hefei, Anhui 230026, China
[3]School of Optical-Electrical and Computer Engineering, University of Shanghai for Science and Technology, Shanghai 200093, China
[4]qwzhan@usst.edu.cn
*zhoulm@hfut.edu.cn

Abstract: Narrow-linewidth circular dichroism (CD) spectroscopy is a promising candidate to push the limits of molecular handedness detection toward a monolayer or even to a single molecule level. Here, we designed a hybrid metasurface consisting of a periodic array of symmetry-breaking dielectric dimers on a gold substrate, which can generate strong CD of 0.44 with an extremely-narrow linewidth of 0.40 nm in the near-infrared. We found that two surface lattice resonance modes can be excited in the designed metasurface, which can be superimposed in the crossing spectral region, enabling a remarkable differential absorption with a high Q-factor for circular polarizations. The multipole decomposition of the resonance modes shows that the magnetic dipole component contributes most to the CD. Our simulation results also show that the CD response of the chiral structure can be engineered by modulating the structural parameters to reach the optimal CD performance. Ultra-narrow-linewidth CD response offered by the proposed metasurface with dissymmetry provides new possibilities towards design of the high-sensitive polarization detecting, chiral sensing and efficient chiral light emitting devices.

1. Introduction

Chirality is an intrinsic property of an object being non-superimposable onto its own mirror image by any symmetry axis [1]. Circular dichroism (CD), as a manifestation of chirality, can be described by the differential absorption of left-handed and right-handed circularly polarized (LCP and RCP) light in spectral response of the chiral structure [2]. For a long time, CD in optical spectra of the chiral molecules has been employed as a useful tool in determination of sugar concentration in food, quality control of drug development relevant process [3] and providing information on the secondary structure and folding properties of proteins [4,5]. But, the inherently weak CD response in natural molecules, along with the limited sensitivity of conventional CD spectroscopic techniques, has imposed a critical limit on the detection sensitivity of CD. Recently, it has been suggested to use the artificial chiral metamaterials and/or metasurfaces to realize the enhanced chirality response [6–13]. These efforts are meant to boost the detection capacity of chiral optical spectroscopy to the single molecule level. Moreover, it has also been demonstrated that the enhanced chiral nanostructures [8–11,14–22] potentially promises a wealth of applications including circularly polarized light detection [23], polarization control [24–28], chirality sensing [29–33], spin-selective perfect light absorption [19,34,35] and circularly polarized light emission [36–40].

#457661 https://doi.org/10.1364/OE.457661
Journal © 2022 Received 7 Mar 2022; revised 6 Apr 2022; accepted 8 Apr 2022; published 25 Apr 2022

Optics EXPRESS

To achieve the efficient light-matter interaction for sensitive detection or light emission, it generally requires the resonant structures to own a high Q-factor [41–47]. However, for a number of the emerged plasmonic chiral nanostructures [18,48], they usually have a large absorption combined with radiation loss, which inevitably induces a relatively broad linewidth in their CD spectra. For instance, the full-width at half-maximum (FWHM) in a designed Z-shaped plasmonic antenna array is about 80 nm [23], and that for a proposed double L-shaped metallic nanorods array is about 50 nm in the near-infrared spectral band [49]. Nevertheless, it should be noted that collective excitations of periodic arrays of nanoparticles or dimers by coupling localized surface resonances to grazing diffraction orders can lead to surface lattice resonances (SLR), which generally have an extremely high Q-factor [50–53]. By further breaking the symmetry of dimer arrays, a narrow-linewidth CD response would be hopefully achieved via the high-Q surface lattice resonances in the chiral metasurface structure.

In this study, we designed a hybrid chiral metasurface formed by an asymmetric dielectric nanorod-dimer array on an optically thick gold substrate. A large CD with an ultra-narrow linewidth has been achieved through adjusting the structural parameters of the proposed symmetry-breaking dimer arrays. We found that two surface lattice resonance modes with high Q-factor can be excited in the orthogonal direction under circularly polarized illumination, whose frequencies can be tuned by changing the structural parameters of dimer to overlap with each other. The superimposed resonant modes allow for the enhanced CD spectral response in absorption with an ultra-narrow linewidth, which has been analyzed theoretically by the multipole decomposition calculations. The optimal CD performance with high Q-factor offered by the designed chiral metasurface paves the way for high-sensitive chiral sensing, circularly-polarized light detection and emission with high performance.

2. Structure design and theory

Schematic of the proposed high-Q chiral metasurface is depicted in Fig. 1. Its unit cell consists of two dielectric elliptical nanorods on an opaque gold substrate, which is periodic in x- and y-directions with the background of air. The parameters of the structure are initially set as follow. The periods of structure in x- and y-direction are the same as $P_x = P_y = 720$ nm, the thickness of gold substrate is $d_0 = 130$ nm. In the dimer, the major-axis of the left rod is fixed along the y-direction with deflection angle $\theta = 0°$, and its minor- and major-axis length is $a_1 = 150$ nm and $b_1 = 400$ nm, respectively. To create the chirality, the symmetry of dimer herein is broken by setting the initial deflection angle of the right rod as $\theta = 6°$ with its minor- and major-axis length of $a_2 = 160$ nm and $b_2 = 406$ nm. The two rods have the same height $h = 460$ nm. Here the refractive index of dielectric rods is chosen as 1.63 and the permittivity of the gold substrate was taken from Johnson and Christy [54]. A RCP or LCP light normally impinges on the structure along the negative z-direction. RCP (LCP) is defined by the rotation direction of the electric field vector as clockwise (counterclockwise) when an observer looks along the wave propagation direction [55]. Full-wave simulations were implemented by using the finite element method (FEM). In the simulations, periodic boundary condition is applied to the unit cell along the x- and y-directions (left/right side), perfectly matched layer (PML) condition is used in the z-direction (up/down side), and meshes are set fine enough ($\lambda/8$ for maximums and $\lambda/12$ for minimums, respectively) that ensures the accuracy of results.

As previously demonstrated, in the dielectric-dimer-arrays on mirror structure, the diffracted orders in the plane of arrays can lead to the extremely-narrow surface lattice resonances [50,51]. The corresponding dispersion equation of this narrow-linewidth surface mode follows the $(\pm 1, 0)$ order diffraction at a grazing angle in air, which can be expressed as

$$|\boldsymbol{k}_{||} + \boldsymbol{G}_{\pm 1,0}| = \frac{2\pi}{\lambda} n_{eff}, \tag{1}$$

Optics EXPRESS

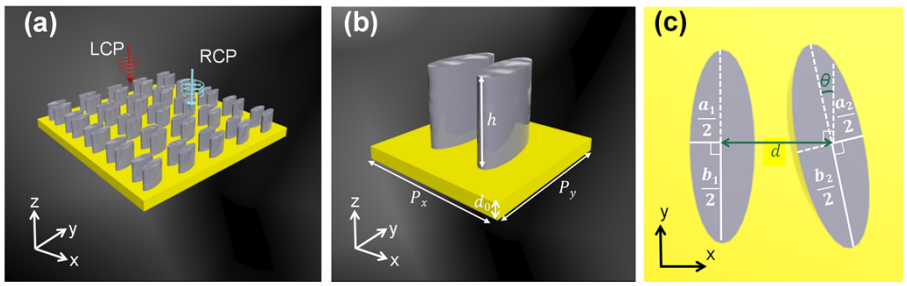

Fig. 1. (a) Illustration of the designed metasurface. (b) Side-view and (c) top-view of the unit cell.

where $\boldsymbol{k}_{\parallel}$ is the in-plane wavevector of incident light, $\boldsymbol{G}$ is the reciprocal lattice vector, λ is the free-space wavelength and n_{eff} is the effective refractive index of the lattice resonance modes. Based on this, to characterize the chiral asymmetry of a system, we can use the CD, which is commonly-used quantity. In terms of optical absorption, it is defined as

$$CD = A_L - A_R, \tag{2}$$

where A_L and A_R are the absorptance of the chiral structure irradiated by the LCP or RCP light, respectively. For a generic two-port system, it is convenient to use the formulism of Jones vectors and matrices to describe its optical response [8]. For the investigation of CD, the Jones matrices in the circular polarization basis are needed, where the reflectivity and transmittivity matrices are expressed as $R_c = \begin{pmatrix} r_{LL} & r_{LR} \\ r_{RL} & r_{RR} \end{pmatrix}$ and $T_c = \begin{pmatrix} t_{LL} & t_{LR} \\ t_{RL} & t_{RR} \end{pmatrix}$, respectively. The subscript L/R herein represents the LCP/RCP. The light absorptance of the structure with the LCP and RCP in Eq. (2) is readily described by

$$A_L = 1 - |r_{LL}|^2 - |t_{LL}|^2 - |r_{RL}|^2 - |t_{RL}|^2, \tag{3}$$

$$A_R = 1 - |r_{RR}|^2 - |t_{RR}|^2 - |r_{LR}|^2 - |t_{LR}|^2. \tag{4}$$

In our structure, the optically thick gold substrate acts as a total reflection mirror. Thus, all the transmission coefficients are zero. In this way, the light absorptance of the structure for the LCP and RCP in Eqs. (3)–(4) is readily described by:

$$A_L = 1 - |r_{LL}|^2 - |r_{RL}|^2, \tag{5}$$

$$A_R = 1 - |r_{RR}|^2 - |r_{LR}|^2. \tag{6}$$

3. Results and discussion

3.1. Optimized chiral structure and its CD performance

The CD performance of the optimized chiral structure under the normal illumination is shown in Fig. 2, where the structural parameters in simulation are the same as those in Section 2. Particularly, Fig. 2(a) indicates the absorption spectra of the structure for LCP and RCP light. We can see that the peak absorptance for the LCP can reach 0.87 while that for the RCP is about 0.61, and the resonance wavelengths of these two peaks deviate a little. Figure 2(b) further displays the CD spectral response of the structure. Notably, it can be observed that an ultra-sharp peak with FWHM of 0.40 nm emerges at the wavelength around 727 nm in CD spectrum, and the maximum CD at which can reach up to 0.44. At the wavelength of left major peak in CD response, the

Optics EXPRESS

absorptivity of the structure reaches the maximum for the LCP, while the absorption peak for the RCP demonstrates a slight redshift to the long-wavelength, accounting for the other weaker CD response on the right. Obviously, high-Q resonance modes with a differential absorption and peak frequency for LCP and RCP give rise to the ultra-sharp-linewidth CD spectral response, as will be discussed in detail later in Section 3.3.

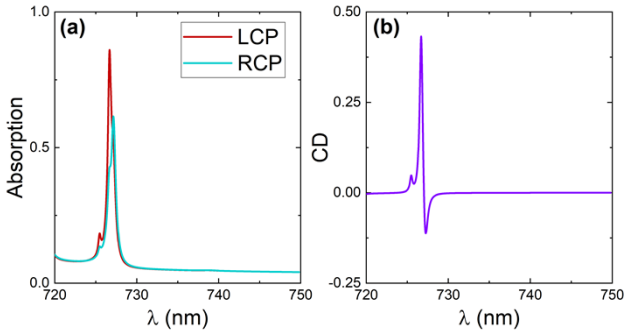

Fig. 2. (a) Absorption spectra of the structure under the normal illumination of LCP and RCP light. (b) The corresponding CD spectral response of the structure.

3.2. Resonantly enhanced absorption with narrow linewidth for circular polarizations

To gain deeper insight into the enhanced absorption response with an extremely-narrow linewidth in the proposed structure, we first studied the dependence of absorption spectra on the center-to-center distance d for the symmetric dimer arrays (Fig. 3(a)).

Here the two rods in dimer have the same dimensions and are symmetric with respect to the $x = 0$ plane, where $a_1 = a_2 = 150$ nm, $b_1 = b_2 = 400$ nm and other parameters in simulation are the same as those in Fig. 2. For the case of $d = 200$ nm, the absorption peaks for LCP and RCP are fully overlapped with each other (Fig. 3(b)), whose absorptivity at peak can reach up to 0.92 at $\lambda = 726$ nm with its linewidth of 0.6 nm. Obviously, no chirality creates in the mirror-symmetric structure. Figure 3(c) further shows the identical absorption spectra of the structure on parameter d for LCP and RCP. We see that two narrow-linewidth resonance modes can be excited in x- and y-direction, respectively. As d increasing, the absorption peaks of these two resonance modes both blue-shift and cross with each other. In the crossing of spectral region, the two modes can degenerate in resonance wavelength, remarkably exhibiting a boost in light absorption. Moreover, Figs. 3(d)–3(g) shows the electric field distributions of the two modes denoted by points P_1 and P_2 ($d = 180$ nm) in Fig. 3(c) for LCP. We see that a 'lifted' electrical field are highly confined at the top of the dimer at P_1, displaying the typical patterns of surface lattice resonance in the dimer arrays [52]; while those at P_2 manifest itself just like a guided resonance in this periodic dimer lattice. Note that the peak absorptivity of the two modes at P_1 and P_2 are only 0.49 and 0.51, respectively. Meanwhile, Figs. 3(h)–3(k) illustrate the electric field distributions of the superimposed modes for LCP and RCP at the intersecting point P. Intriguingly, it can be observed that the field patterns of this resonance mode at the crossing point for LCP and RCP resemble with each other, displaying a hybrid nature from that at P_1 and P_2. Thanks to the enlarged mode volume for the superimposed mode at the crossing point (Figs. 3(h)–3(k)), light absorption of the hybrid mode at the crossing spectral region is tremendously enhanced up to more than 0.92, while the linewidth of this hybrid mode remains as narrow as 0.6 nm. On the basis of it, by further breaking the symmetry of dimer, a high-Q circular dichroism is expected to be realized through this unique high-Q degenerate mode in the proposed metasurface.

Optics EXPRESS

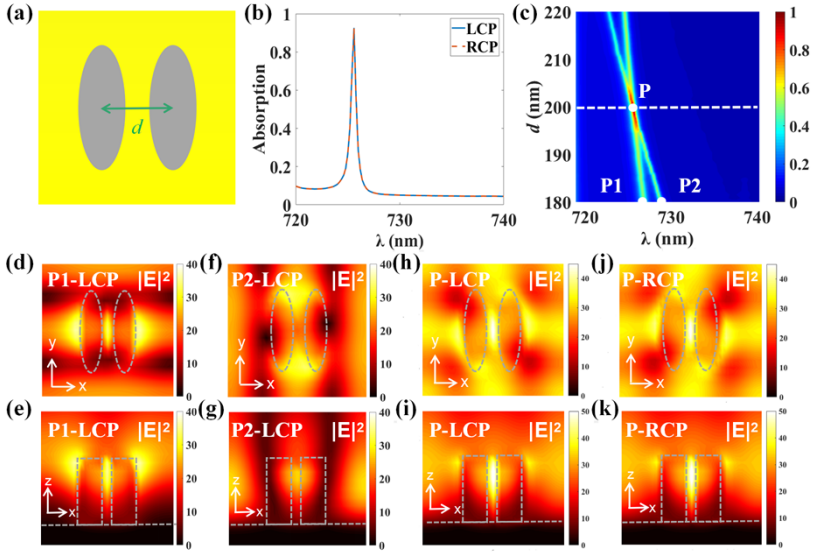

Fig. 3. (a) Illustration of the unit cell of mirror-symmetric dimer arrays. (b) Absorption response of the symmetric structure for LCP (blue solid) and RCP (red dashed). (c) Absorption spectra of the structure as a function of the parameter d for LCP and RCP. (d)-(g) $|E|^2$ distributions of the structure at the points of P_1 and P_2 in (c) with d = 180 nm for LCP. (h)-(k) $|E|^2$ distributions of the structure at point of P with d = 200 nm for LCP and RCP, respectively. First and second row in panels of (d)-(k) illustrate the $|E|^2$ distribution in xy-plane 5 nm below the top of dimer and y = 0 plane, respectively.

3.3. *Dependence of CD on the structural asymmetry and its optimization process*

Note that the CD of metasurface can be created by simultaneously breaking both the n-fold rotational (n>2) and mirror symmetries [56]. The elements in Jones matrixes R and T for circular polarization should be naturally related to the symmetry of the structure, which in turn will impact the CD response of the structure. Symmetry-breaking for the proposed arrays of dimers can be implemented by simply changing the deflection angle, length of major- or/and minor-axis of one rod, which shall be optimized to reach the maximum CD in this chiral system.

We first investigated the dependence of CD on the deflection angle θ of the right rod, where other parameters in dimer arrays retain the same as those in Fig. 3(b) with a high light absorption. Figures 4(a)–4(b) shows the absorption spectra on the deflection angle θ for LCP and RCP, respectively. The corresponding CD spectrum as a function of the deflection angle θ is given in Fig. 4(c). Particularly, as θ goes up, the peak absorptivity of the structure for the LCP increases first to the maximum at about 2° and then decreases, and the absorption peak blue-shifts to the short wavelength slowly, as shown in Figs. 4(d)–4(e). In contrast, the peak absorptivity for the RCP decreases rapidly, which is companied by a red-shift in resonance wavelength. Obviously, as the increasing of the deflection angle θ, the differential peak absorptivity in combination with the deviation of resonance wavelength for the high-Q resonances with LCP and RCP leads to the sharp CD spectra. As displayed in Fig. 4(c), the CD spectrum ends up with one major peak and one dip, where the CD can reach its maximum (absolute value) of 0.38 approximately at the deflection angle of 6°.

Then, by fixing the deflection angle at θ = 6°, Figs. 5(a)–5(b) show the absorption spectra of the structure as a function of the parameter a_2 for LCP and RCP light, respectively, and the

Optics EXPRESS

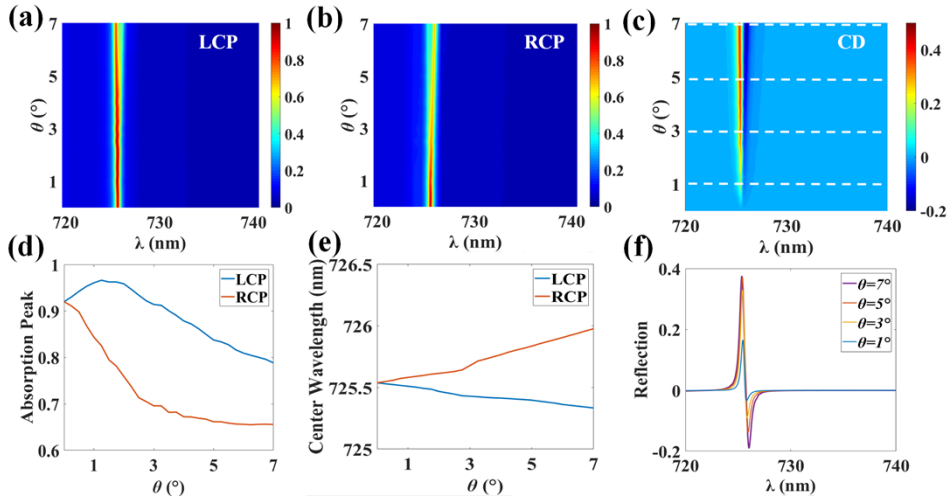

Fig. 4. Absorption spectra of the structure with respect to the deflection angle θ of the right rod for (a) LCP and (b) RCP, with its CD spectra as a function of θ shown in (c). Dependence of (d) the maximum absorptance and (e) the resonant wavelength on deflection angle θ for LCP (light blue) and RCP (red) in (a)-(b). (f) Typical CD spectral lines at $\theta = 1°$, 3°, 5°, 7° in (c).

corresponding CD spectra are given in Fig. 5(c). We can see, with increasing of the minor-axis-length a_2, two narrow-linewidth resonance modes in the structure both show a red-shift in absorption peak. Moreover, a notable spectral overlap featuring an enhanced absorption for the two resonances can be clearly observed in the absorption spectra, which is within range of a_2 from 140 nm to 170 nm. The maximum absorptivity of this superimposed modes for LCP can reach 0.85 at the minor-axis-length a_2 of 155 nm. Meanwhile, it is also seen that the absorption spectra on the parameter a_2 for the RCP display the similar trend. The absorptivity reaches its maximum at the crossing of spectral region, but the peak wavelength of the resonant mode deviates a little from that of the LCP with a relatively weaker absorptivity. The maximum CD herein reaches 0.42 at a_2 = 160 nm, as shown in Fig. 5(c).

Moreover, the absorption spectra of the structure on parameter b_2 are shown in Figs. 5(d)–5(e) for LCP and RCP, respectively, where other parameters of the structure keep the same as those in Fig. 5(a). And its CD spectra are indicated in Fig. 5(f). Resembling the evolution of the spectra in Fig. 5(a)–5(b), with the increasing of the major-axis-length b_2, two resonance modes in the structure similarly display a red shift. Spectral crossing with an enhanced absorption for the two resonance modes also can be observed in the absorption spectra for both LCP and RCP. As demonstrated in Fig. 5(f), CD reaches its maximum of 0.44 at b_2 = 406 nm.

3.4. *Multipole analysis of the resonant absorption response in the chiral structure*

To better understand the origin of the optical chirality response in the proposed structure, the $|E|^2$ field distributions at the peak wavelengths of 726.7 nm and 727.2 nm in Fig. 2(a) for LCP and RCP are shown in Figs. 6(a)–6(d). Specifically, Figs. 6(a)–6(b) show the distributions of electric field intensity and displacement current vectors in the xy-plane 5 nm below the top of dimer for LCP and RCP, respectively. And those in the y = 0 plane across the center of the two rods are illustrated in Figs. 6(c)–6(d). It can be observed that the enhanced fields are highly confined at the top of dielectric dimer, clearly exhibiting the characteristics of the surface lattice resonances for LCP and RCP. Meanwhile, it shall be further noted that the field distributions of the two superimposed resonance modes in the dimer for LCP and RCP are dramatically different. That is,

Optics EXPRESS

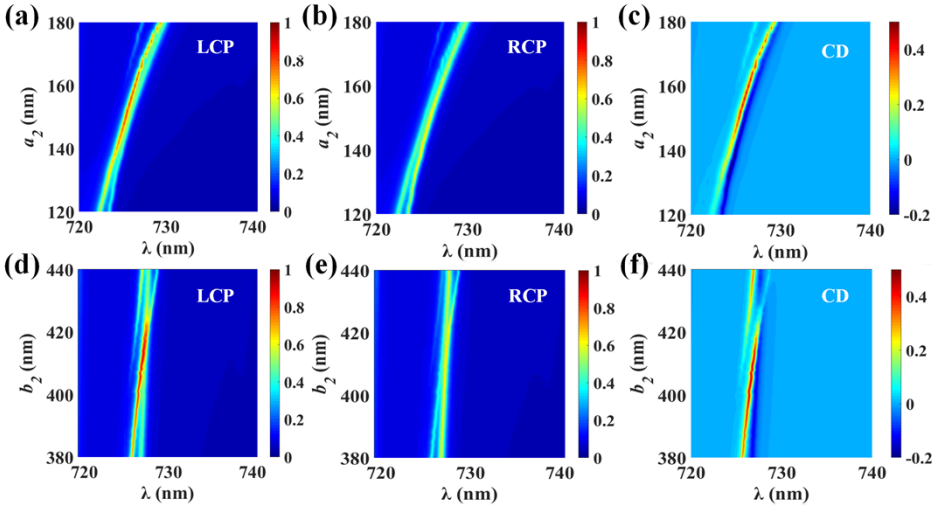

Fig. 5. Absorption spectra of the structure with respect to the minor-axis-length a_2 of the right rod for (a) LCP and (b) RCP. (c) CD spectra as a function of the minor-axis-length a_2. (d)-(f) The same as (a)-(c) but for the different major-axis-length b_2 of the right rod.

the field confinement for LCP is mostly along the y-direction through the gap, while the 'lifted' field for RCP is localized along the x-direction across the dimer (see Figs. 6(a)–6(b)). Thereby, the different modal field distributions for LCP and RCP give rise to the spin-selective absorption response in this chiral resonant regime.

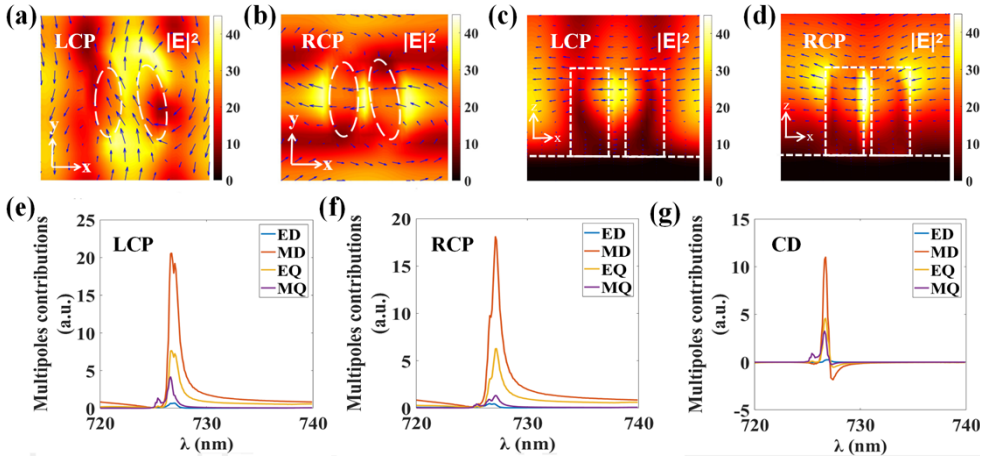

Fig. 6. (a)-(b) The $|E|^2$ distributions in xy-plane of the structure 5 nm below the top of dimer for LCP and RCP, (c)-(d) $|E|^2$ distributions in $y = 0$ plane, where the displacement current vectors are indicated by blue arrows. (e)-(f) Multipole decomposition of the resonances in the structure under the excitation of LCP and RCP, respectively. (g) The contribution of multipole in CD.

To further learn the components of the superposition state in the surface lattice resonance, here we have calculated the moments of excited multipoles in the structure at the different incident wavelength, and shown the scattering light contribution by different multipoles in Figs. 6(e)–6(f).

Optics EXPRESS

The multipole decomposition in the structure has been calculated by the formula [57] as

$$\mathbf{p} = \int \mathbf{P} j_0(kr) d\mathbf{r} + \frac{k^2}{10} \int \{[\mathbf{r}\cdot\mathbf{P}]\mathbf{r} - \frac{1}{3} r^2 \mathbf{P}\} \frac{15 j_2(kr)}{(kr)^2} d\mathbf{r}, \tag{7}$$

$$\mathbf{m} = -\frac{i\omega}{2} \int [\mathbf{r}\times\mathbf{P}] \frac{3 j_1(kr)}{kr} d\mathbf{r}, \tag{8}$$

$$\begin{aligned} \hat{Q} = &\int \{3(\mathbf{r}\otimes\mathbf{P} + \mathbf{P}\otimes\mathbf{r}) - 2[\mathbf{r}\cdot\mathbf{P}]\hat{U}\} \times \tfrac{3 j_1(kr)}{kr} d\mathbf{r} \\ &+ 6k^2 \int \{5\mathbf{r}\otimes\mathbf{r}[\mathbf{r}\cdot\mathbf{P}] - (\mathbf{r}\otimes\mathbf{P} + \mathbf{P}\otimes\mathbf{r}) r^2 - r^2[\mathbf{r}\cdot\mathbf{P}]\hat{U}\} \tfrac{j_3(kr)}{(kr)^3} d\mathbf{r}, \end{aligned} \tag{9}$$

$$\hat{M} = \frac{\omega}{3i} \int \{[\mathbf{r}\times\mathbf{P}]\otimes\mathbf{r} + \mathbf{r}\otimes[\mathbf{r}\times\mathbf{P}]\} \frac{15 j_2(kr)}{(kr)^2} d\mathbf{r}. \tag{10}$$

Here, p, m, $\hat{Q}$, $\hat{M}$ in Eqs. (7)–(10) are the multipole moments in the Cartesian representation, denoting the electric dipole (ED), the magnetic dipole (MD), the electric quadrupole (EQ) and the magnetic quadrupole (MQ), respectively. In addition, P represents the light-induced polarization, $\hat{U}$ is the 3-dimentional unit tensor, j_n denotes the n-th order spherical Bessel function, and k is the wave number in air. Based on the simulated results of the electromagnetic field and induced polarization **P**, the multipole moments can be calculated through Eqs. (7)–(10), as shown in Figs. 6(e)–6(f). It can be seen that MD, EQ and MQ have major contributions to the absorption for the LCP light, whereas only MD, EQ for the RCP light. We further plot the CD spectrum for the different multipoles in Fig. 6(g). It clearly demonstrates that MD, EQ and MQ all contribute to, but the MD dominates the resulting narrow-linewidth CD response in this chiral metasurface.

Moreover, it is noted that chiral metasurface with narrow spectral linewidth (thus, high-Q) can be of the crucial importance for improving the resolution of imaging, efficiency of photoelectric detection and sensitivity of biomolecular detection. Here we list the central wavelength λ, FWHM $\Delta\lambda$ and Q values of some recently published works in Table 1. It can be seen that FWHM and Q value in this design is better than most of the existing works in the near-infrared frequencies, which makes it promising for various chirality-related applications.

Table 1. Central Wavelengths, FWHMs and Q-Values of Several Chiral Structures in Published Works

Structure	λ	FWHM $\Delta\lambda$	Q
This work	726 nm	0.4 nm	1815
Hook structure [34]	620 nm	200 nm	3.1
Z-shape antenna array [23]	1370 nm	80 nm	17.13
Double L-shaped nanorods [49]	730 nm	50 nm	14.6
Two unaligned nanorods [58]	725 nm	20 nm	36.25
Z-shaped GST resonators [59]	1800 nm	80 nm	22.5

4. Conclusions

In summary, we proposed and theoretically investigated a chiral metasurface based on the arrays of asymmetric dielectric dimers on a gold substrate, whose maximum CD in absorption can reach 0.44 with an ultra-narrow spectral linewidth of 0.40 nm. Our simulation results show the metasurface supports two resonant surface modes with high Q-factors, which can be tuned to be superimposed with each other. Moreover, the sharp linewidth of CD in the structure is enabled by the spin-selective high-Q resonance modes with a differential absorptivity and the deviation of the resonance wavelength for LCP and RCP. Additionally, the multipole decomposition of the

Optics EXPRESS

excited resonant modes further reveals that the magnetic dipole component contributes most to the strong CD in this regime. A straight-forward optimization strategy has been implemented to reach the maximum CD while still keeping the characteristics of ultra-narrow linewidth and high-Q in the designed chiral metasurface. Our findings can find potential applications including high-sensitive polarization detection, chiral sensing and efficient chiral light emitting.

Funding. National Natural Science Foundation of China (62075053, 92050202, U20A20216); Fundamental Research Funds for the Central Universities (PA2020GDKC0024).

Acknowledgments. We thank Dr. Xiaolin Chen for the helpful discussions.

Disclosures. The authors declare no conflicts of interest.

Data Availability. Data underlying the results presented in this paper are not publicly available at this time but may be obtained from the authors upon reasonable request.

References

1. L. W. T. Kelvin, *Baltimore lectures on molecular dynamics and the wave theory of light* (C. J. Clay and Sons, 1904).
2. L. D. Barron, *Molecular Light Scattering and Optical Activity*, 2nd ed. (Cambridge University, 2004).
3. N. Berova, K. Nakanishi, and R. W. Woody, *Circular Dichroism: Principles and Applications*, 2nd ed. (Wiley-VCH, 2000).
4. N. J. Greenfield, "Using circular dichroism spectra to estimate protein secondary structure," Nat. Protoc. **1**(6), 2876–2890 (2006).
5. F. U. Hartl, "Protein Misfolding Diseases," Annu. Rev. Biochem. **86**(1), 21–26 (2017).
6. J. K. Gansel, M. Thiel, M. S. Rill, M. Decker, K. Bade, V. Saile, G. von Freymann, S. Linden, and M. Wegener, "Gold helix photonic metamaterial as broadband circular polarizer," Science **325**(5947), 1513–1515 (2009).
7. E. Plum, X. X. Liu, V. A. Fedotov, Y. Chen, D. P. Tsai, and N. I. Zheludev, "Metamaterials: optical activity without chirality," Phys. Rev. Lett. **102**(11), 113902 (2009).
8. Z. Wang, F. Cheng, T. Winsor, and Y. Liu, "Optical chiral metamaterials: a review of the fundamentals, fabrication methods and applications," Nanotechnology **27**(41), 412001 (2016).
9. Y. Chen, J. Gao, and X. Yang, "Chiral Metamaterials of Plasmonic Slanted Nanoapertures with Symmetry Breaking," Nano Lett. **18**(1), 520–527 (2018).
10. Z. Huang, K. Yao, G. Su, W. Ma, L. Li, Y. Liu, P. Zhan, and Z. Wang, "Graphene-metal hybrid metamaterials for strong and tunable circular dichroism generation," Opt. Lett. **43**(11), 2636–2639 (2018).
11. M. V. Gorkunov, A. A. Antonov, and Y. S. Kivshar, "Metasurfaces with Maximum Chirality Empowered by Bound States in the Continuum," Phys. Rev. Lett. **125**(9), 093903 (2020).
12. A. Overvig, N. Yu, and A. Alù, "Chiral Quasi-Bound States in the Continuum," Phys. Rev. Lett. **126**(7), 073001 (2021).
13. M. V. Gorkunov, A. A. Antonov, V. R. Tuz, A. S. Kupriianov, and Y. S. Kivshar, "Bound States in the Continuum Underpin Near-Lossless Maximum Chirality in Dielectric Metasurfaces," Adv. Opt. Mater. **9**(19), 2100797 (2021).
14. M. Hentschel, M. Schäferling, T. Weiss, N. Liu, and H. Giessen, "Three-Dimensional Chiral Plasmonic Oligomers," Nano Lett. **12**(5), 2542–2547 (2012).
15. B. Frank, X. Yin, M. Schäferling, J. Zhao, S. M. Hein, P. V. Braun, and H. Giessen, "Large-Area 3D Chiral Plasmonic Structures," ACS Nano **7**(7), 6321–6329 (2013).
16. X. Yin, M. Schäferling, B. Metzger, and H. Giessen, "Interpreting Chiral Nanophotonic Spectra: The Plasmonic Born–Kuhn Model," Nano Lett. **13**(12), 6238–6243 (2013).
17. A. Yokoyama, M. Yoshida, A. Ishii, and Y. K. Kato, "Giant Circular Dichroism in Individual Carbon Nanotubes Induced by Extrinsic Chirality," Phys. Rev. X **4**(1), 011005 (2014).
18. Y. Chen, W. Du, Q. Zhang, O. Ávalos-Ovando, J. Wu, Q.-H. Xu, N. Liu, H. Okamoto, A. O. Govorov, Q. Xiong, and C.-W. Qiu, "Multidimensional nanoscopic chiroptics," Nat. Rev. Phys. **4**(2), 113–124 (2022).
19. K. Zhang, Y. Liu, S. Li, F. Xia, and W. Kong, "Actively tunable bi-functional metamirror in a terahertz band," Opt. Lett. **46**(3), 464–467 (2021).
20. J. Wu, X. Xu, X. Su, S. Zhao, C. Wu, Y. Sun, Y. Li, F. Wu, Z. Guo, H. Jiang, and H. Chen, "Observation of Giant Extrinsic Chirality Empowered by Quasi-Bound States in the Continuum," Phys. Rev. Appl. **16**(6), 064018 (2021).
21. L. Ouyang, W. Wang, D. Rosenmann, D. A. Czaplewski, J. Gao, and X. Yang, "Near-infrared chiral plasmonic metasurface absorbers," Opt. Express **26**(24), 31484–31489 (2018).
22. M. S. Mahmud, D. Rosenmann, D. A. Czaplewski, J. Gao, and X. Yang, "Chiral plasmonic metasurface absorbers in the mid-infrared wavelength range," Opt. Lett. **45**(19), 5372–5375 (2020).
23. W. Li, Z. J. Coppens, L. V. Besteiro, W. Wang, A. O. Govorov, and J. Valentine, "Circularly polarized light detection with hot electrons in chiral plasmonic metamaterials," Nat. Commun. **6**(1), 8379 (2015).
24. Y. Zhao, M. A. Belkin, and A. Alù, "Twisted optical metamaterials for planarized ultrathin broadband circular polarizers," Nat. Commun. **3**(1), 870 (2012).
25. S. Wang, L. Kang, and D. H. Werner, "Active Terahertz Chiral Metamaterials Based on Phase Transition of Vanadium Dioxide (VO2)," Sci. Rep. **8**(1), 189 (2018).

Optics EXPRESS

26. D. Ma, Z. Li, Y. Zhang, W. Liu, H. Cheng, S. Chen, and J. Tian, "Giant spin-selective asymmetric transmission in multipolar-modulated metasurfaces," Opt. Lett. **44**(15), 3805–3808 (2019).
27. X. Luo, F. Hu, and G. Li, "Dynamically reversible and strong circular dichroism based on Babinet-invertible chiral metasurfaces," Opt. Lett. **46**(6), 1309–1312 (2021).
28. G. Cao, H.-X. Xu, L.-M. Zhou, Y. Deng, Y. Zeng, S. Dong, Q. Zhang, Y. Li, H. Yang, Q. Song, X. Liu, Y. Li, and C.-W. Qiu, "Infrared metasurface-enabled compact polarization nanodevices," Mater. Today **50**(1), 499–515 (2021).
29. F. Lu, Y. Tian, M. Liu, D. Su, H. Zhang, A. O. Govorov, and O. Gang, "Discrete nanocubes as plasmonic reporters of molecular chirality," Nano Lett. **13**(7), 3145–3151 (2013).
30. J. Feis, D. Beutel, J. Kopfler, X. Garcia-Santiago, C. Rockstuhl, M. Wegener, and I. Fernandez-Corbaton, "Helicity-Preserving Optical Cavity Modes for Enhanced Sensing of Chiral Molecules," Phys. Rev. Lett. **124**(3), 033201 (2020).
31. T. Kakkar, C. Keijzer, M. Rodier, T. Bukharova, M. Taliansky, A. J. Love, J. J. Milner, A. S. Karimullah, L. D. Barron, N. Gadegaard, A. J. Lapthorn, and M. Kadodwala, "Superchiral near fields detect virus structure," Light: Sci. Appl. **9**(1), 195 (2020).
32. L. A. Warning, A. R. Miandashti, L. A. McCarthy, Q. Zhang, C. F. Landes, and S. Link, "Nanophotonic Approaches for Chirality Sensing," ACS Nano **15**(10), 15538–15566 (2021).
33. Y. Chen, C. Zhao, Y. Zhang, and C. W. Qiu, "Integrated Molar Chiral Sensing Based on High-Q Metasurface," Nano Lett. **20**(12), 8696–8703 (2020).
34. W. Liu, L. Mei, Y. Li, L. Yu, Z. Lai, T. Yu, and H. Chen, "Controlling the spin-selective absorption with two-dimensional chiral plasmonic gratings," Opt. Lett. **44**(23), 5868–5871 (2019).
35. Z. Shen, X. Fang, S. Li, W. Yin, L. Zhang, and X. Chen, "Terahertz spin-selective perfect absorption enabled by quasi-bound states in the continuum," Opt. Lett. **47**(3), 505–508 (2022).
36. M. Cotrufo, C. I. Osorio, and A. F. Koenderink, "Spin-Dependent Emission from Arrays of Planar Chiral Nanoantennas Due to Lattice and Localized Plasmon Resonances," ACS Nano **10**(3), 3389–3397 (2016).
37. B. Peng, Ş. K. Özdemir, M. Liertzer, W. Chen, J. Kramer, H. Yılmaz, J. Wiersig, S. Rotter, and L. Yang, "Chiral modes and directional lasing at exceptional points," Proc. Natl. Acad. Sci. **113**(25), 6845–6850 (2016).
38. T. Matsukata, G. F. Javier de Abajo, and T. Sannomiya, "Chiral Light Emission from a Sphere Revealed by Nanoscale Relative-Phase Mapping," ACS Nano **15**(2), 2219–2228 (2021).
39. K. Q. Le, S. Hashiyada, M. Kondo, and H. Okamoto, "Circularly Polarized Photoluminescence from Achiral Dye Molecules Induced by Plasmonic Two-Dimensional Chiral Nanostructures," J. Phys. Chem. C **122**(43), 24924–24932 (2018).
40. I. C. Seo, Y. Lim, S.-C. An, B. H. Woo, S. Kim, J. G. Son, S. Yoo, Q. H. Park, J. Y. Kim, and Y. C. Jun, "Circularly Polarized Emission from Organic–Inorganic Hybrid Perovskites via Chiral Fano Resonances," ACS Nano **15**(8), 13781–13793 (2021).
41. K. Koshelev, S. Lepeshov, M. Liu, A. Bogdanov, and Y. Kivshar, "Asymmetric Metasurfaces with High-Q Resonances Governed by Bound States in the Continuum," Phys. Rev. Lett. **121**(19), 193903 (2018).
42. Y. Zhang, W. Liu, Z. Li, Z. Li, H. Cheng, S. Chen, and J. Tian, "High-quality-factor multiple Fano resonances for refractive index sensing," Opt. Lett. **43**(8), 1842–1845 (2018).
43. X. Chen and W. Fan, "Ultrahigh-Q toroidal dipole resonance in all-dielectric metamaterials for terahertz sensing," Opt. Lett. **44**(23), 5876–5879 (2019).
44. J. Hu, W. Liu, W. Xie, W. Zhang, E. Yao, Y. Zhang, and Q. Zhan, "Strong coupling of optical interface modes in a 1D topological photonic crystal heterostructure/Ag hybrid system," Opt. Lett. **44**(22), 5642–5645 (2019).
45. J. Tian, Q. Li, P. A. Belov, R. K. Sinha, W. Qian, and M. Qiu, "High-Q All-Dielectric Metasurface: Super and Suppressed Optical Absorption," ACS Photonics **7**(6), 1436–1443 (2020).
46. X. Zhang, R. T. Yan, and T. J. Cui, "High-FoM Resonance in Single Hybrid Plasmonic Resonator Via Electromagnetic Modal Interference," IEEE Trans. Antennas Propag. **68**(8), 6447–6451 (2020).
47. D. Lee, S. So, G. Hu, M. Kim, T. Badloe, H. Cho, J. Kim, H. Kim, C.-W. Qiu, and J. Rho, "Hyperbolic metamaterials: fusing artificial structures to natural 2D materials," eLight **2**(1), 1 (2022).
48. V. K. Valev, J. J. Baumberg, C. Sibilia, and T. Verbiest, "Chirality and chiroptical effects in plasmonic nanostructures: fundamentals, recent progress, and outlook," Adv. Mater. **25**(18), 2517–2534 (2013).
49. Z. Jing, Y. Bai, T. Wang, H. Ullah, Y. Li, and Z. Zhang, "Enhanced circular dichroism of double L-shaped nanorods induced by gap plasmon coupling," J. Opt. Soc. Am. B **36**(10), 2721–2726 (2019).
50. V. G. Kravets, F. Schedin, and A. N. Grigorenko, "Extremely narrow plasmon resonances based on diffraction coupling of localized plasmons in arrays of metallic nanoparticles," Phys. Rev. Lett. **101**(8), 087403 (2008).
51. S. R. K. Rodriguez, A. Abass, B. Maes, O. T. A. Janssen, G. Vecchi, and J. G. Rivas, "Coupling Bright and Dark Plasmonic Lattice Resonances," Phys. Rev. X **1**(2), 021019 (2011).
52. X. Ao, "Surface mode with large field enhancement in dielectric-dimer-on-mirror structures," Opt. Lett. **43**(5), 1091–1094 (2018).
53. V. G. Kravets, A. V. Kabashin, W. L. Barnes, and A. N. Grigorenko, "Plasmonic Surface Lattice Resonances: A Review of Properties and Applications," Chem. Rev. **118**(12), 5912–5951 (2018).
54. P. B. Johnson and R. W. Christy, "Optical Constants of the Noble Metals," Phys. Rev. B **6**(12), 4370–4379 (1972).
55. Z. Wang, H. Jia, K. Yao, W. Cai, H. Chen, and Y. Liu, "Circular Dichroism Metamirrors with Near-Perfect Extinction," ACS Photonics **3**(11), 2096–2101 (2016).

Optics EXPRESS

56. L. Jing, Z. Wang, Y. Yang, B. Zheng, Y. Liu, and H. Chen, "Chiral metamirrors for broadband spin-selective absorption," Appl. Phys. Lett. **110**(23), 231103 (2017).
57. P. D. Terekhov, V. E. Babicheva, K. V. Baryshnikova, A. S. Shalin, A. Karabchevsky, and A. B. Evlyukhin, "Multipole analysis of dielectric metasurfaces composed of nonspherical nanoparticles and lattice invisibility effect," Phys. Rev. B **99**(4), 045424 (2019).
58. Y. Li, Y. Bai, Z. Zhang, A. Abudukelimu, Y. Ren, I. Muhammad, Q. Li, and Z. Zhang, "Enhanced circular dichroism of plasmonic chiral system due to indirect coupling of two unaligned nanorods with metal film," Appl. Opt. **60**(23), 6742–6747 (2021).
59. C. Ding, G. Rui, B. Gu, Q. Zhan, and Y. Cui, "Phase-change metasurface with tunable and switchable circular dichroism," Opt. Lett. **46**(10), 2525–2528 (2021).